Journal of Neuroinflammation

RESEARCH

Open Access

Single-cell and spatial transcriptomics analyses reveal tumor microenvironment–driven proliferation of NF2-associated vestibular schwannomas

Ying Wang[1,2†], Gang Xu[3,4†], Yuan Ren[5], Tao Pan[6], Ya Zhang[6], Yanan Liu[7], Zhijun Yang[2], Zheng Zhao[8], Peng Li[2], Minjun Yan[2], Chao Zhang[2], Bo Wang[2], Xin Ma[2], Yongsheng Li[7,9,10], Juan Xu[3,4*] and Pinan Liu[1,2*]

Abstract

The tumor microenvironment (TME) is crucial for tumor formation and progression, but its specific impact on NF2-related tumors has not been well described. The aim of this study was to analyze the differences in the TME among NF2-related schwannomatosis (NF2-SWN) patients with different clinical phenotypes, explore the reasons for these differences, and identify targets for treatment while gaining a deeper understanding of the pathogenesis of the disease. 20 vestibular schwannomas (VSs) from 20 clinically diagnosed NF2-SWN patients, including 11 milder patients (Gardner) and 9 severe patients (Wishart), were analyzed. Single-cell sequencing, TCR sequencing, spatial transcriptomics analysis, multiplex immunofluorescence, immunohistochemistry, and cell experiments were performed to compare the TME of Gardner and Wishart and to elucidate the mechanisms underlying these differences. Our results revealed that NF2-VS consist of 12 significant cell subpopulations, with Gardner and Wishart presenting distinct TME. Wishart exhibited more pronounced immune suppression. Conversely, $CD8^+$ T cells from Gardner demonstrated potential for clonal proliferation. In macrophages, a subtype exhibited higher capacity of angiogenesis and high inflammatory cytokine activity was identified in Wishart, suggested its role in promoting tumor progression. Moreover, we found fibroblasts in Wishart showed excessive stromal deposition, potentially indicated the existence of immunologic barrier. Receptor–ligand pair analysis revealed that Schwann cells in Wishart regulate immune cell activity via pleiotrophin (PTN), PTN positivity promotes anti-inflammatory cytokine activity, contributing to the formation of an immunosuppressive microenvironment to promote tumor progression. In summary, our study provides an in-depth analysis of the TME of NF2-VS, revealing the differences between Wishart and Gardner. Our study explains how Schwann cells influence the immune landscape to promote tumor

†Ying Wang and Gang Xu contributed equally to this work.

*Correspondence:
Juan Xu
xujuanbiocc@ems.hrbmu.edu.cn
Pinan Liu
pinanliu@ccmu.edu.cn

Full list of author information is available at the end of the article

development and clarifies the role of the TME in NF2-SWN progression, establishing a theoretical and experimental foundation for future immunotherapeutic strategies for NF2-SWN.

Keywords NF2-associated vestibular schwannoma, TME, Cell–cell interaction, Single-cell multiomics

Introduction

NF2-related schwannomatosis (NF2-SWN) [1] is a rare autosomal dominant disorder characterized by multiple tumors in the nervous system, with bilateral vestibular schwannomas(NF2-VS) as a hallmark feature [2]. NF2-related tumors are benign, but their high risk of surgical removal [3, 4] and frequent occurrence of multiple recurrent tumors [5, 6] urgent need new and effective treatment options.

Years of tumor research have demonstrated that genetic alterations are essential but not sufficient for the initiation and progression of tumors. TME cells and their secreted molecules are now recognized as playing crucial roles in the pathogenesis of tumor and thus represent attractive therapeutic targets. Our previous findings suggest that NF2-SWN patients are in an immunosuppressed state [7], targeting PD-L1 may restore the function of tumor-infiltrating lymphocytes and induce apoptosis to inhibit tumor proliferation [8]. This possibility highlights the need for a comprehensive exploration of the TME in the development of NF2-VS, which will be crucial for development of effective anti-tumor treatments for NF2-SWN patients.

To obtain a comprehensive understanding of the TME in the development of NF2-VS, we carefully analyzed 11 NF2-VS samples from Gardner and 9 samples from Wishart. We comprehensively characterized the transcriptomic features of malignant cells, immune cells, and stromal cells in the TME of NF2-VS among Gardner and Wishart, as well as the dynamic changes in cell proportions, the heterogeneity of cell subtypes, and intercellular interactions. This study contributes to a better understanding of the TME composition of NF2-VS, the differences in the TME of Gardner and Wishart, and the effects of these differences on tumor progression and the potential mechanisms involved. These findings provide a foundation for further understanding the pathogenesis of this disease and developing better treatment strategies.

Results

Single-cell transcriptomic profiling of NF2-VS

To systematically analyze the role of TME in the development of NF2-SWN, we conducted scRNA-seq and paired T-cell receptor sequencing (scTCR-seq) on a comprehensive set of 20 VSs collected from 20 NF2-SWN patients who underwent surgical intervention. This cohort included 11 Gardner and 9 Wishart (Supplementary Table 1). Furthermore, we processed two fresh VS samples from two NF2-SWN patients—one Gardner and one Wishart—utilizing spatial transcriptomics to explore spatial characteristics (Fig. 1A-B).

Following rigorous filtering, we retained 145,771 high-quality individual cells for subsequent analysis. These cells underwent normalization of gene expression, followed by principal component analysis (PCA), and were subsequently partitioned into 29 distinct subgroups (Supplementary Fig. 1A-B). We manually annotated these clusters, assigning them to 12 known cell lineages (Fig. 1C and Supplementary Fig. 1C-D), including smooth muscle cells, cycling cells, B cells, mast cells, fibroblasts, neutrophils, dendritic cells (DCs), monocytes, Schwann cells, T and NK cells, macrophages, and endothelial cells. The distribution of each cell type is illustrated in a bar chart (Supplementary Fig. 1E). All cell types were present across the 20 patients; however, the proportions of each lineage varied significantly among individuals, highlighting the tumor heterogeneity inherent in NF2-VS. Furthermore, we subclustered the proliferating cells and identified three distinct types: T cells, myeloid cells, and Schwann cells (Fig. 1C and Supplementary Fig. 1F). Through comparative analysis, we discovered that the proportion of cycling cells in Gardner was significantly greater than that in Wishart across all three cell populations. These findings may reflect immune turnover or homeostatic activation in Gardner. Moreover, to further elucidate the multicellular ecosystems of Gardner and Wishart, we conducted six-plex immunohistochemical staining and further supported the observations. (Fig. 1D).

To gain deeper insights into the spatial characteristics of NF2-VS, we conducted spatial transcriptome sequencing on two fresh samples—one from Gardner and one from Wishart (Fig. 1E and Supplementary Fig. 1G). Cell types were obtained through deconvolution based on sc-RNAseq data. The results demonstrate that the abundances of the cell types we identified were also validated at the spatial level. T cells, macrophages, and fibroblasts account for a relatively large proportion and exhibit heterogeneity across regions and different phenotypes. The above results present the overall composition of the TME in both Gardner and Wishart and suggest that the TME exhibits significant heterogeneity.

GZMK$^+$ and GZMB$^+$ CD8 T-cell subsets are enriched in Gardner

We sub-clustered 30,889 T cells and NK cells into 18 distinct subgroups based on the expression of common markers including naïve T subtype, 3 CD4 subtypes, 7

CD8 subtypes, NKT subtype, two non-common T subtypes (gdT and MAIT) and two NK subtypes (Fig. 2A-B, Supplementary Fig. 2A and Supplementary Table 2). Confused subtypes were excluded with dowstream analysis (T_Macrophage, T_Schwann). Intriguingly, the proportion of the CD8_GZMK_TXNIP subpopulation ($p = 0.046$) was significantly enriched in Gardner (Fig. 2C, Supplementary Fig. 2B-C), additionally, the cytotoxic CD8_GZMB subpopulation is also enriched in Gardner (Fig. 2C). Two GZMK$^+$CD8 T subtypes were identified, differential expressed genes showed that CD8_GZMK_TXNIP exhibited higher expression of cytotoxicity-associated genes (e.g., GNLY) compare to subtype CD8_GZMK_CD74(Supplementary Fig. 2D). Further functional enrichment analysis revealed that CD8_GZMK_TXNIP subpopulation was associated with cytokine production, cell killing and cytotoxicity, consistent with the limited or intermediate cytotoxic potential reported for GZMK$^+$ CD8 T cells (Supplementary Fig. 2E). Pseudotime analysis further confirmed that CD8_GZMK_TXNIP cells were in the terminal differentiation stage compare to CD8_GZMK_CD74, which indicated higher cytotoxic potential. Whereas the CD8$^+$ T cell subpopulations with increased abundance in Wishart (CD8_naiveT and CD8_SOX4) were enriched in the early stages of differentiation (Supplementary Fig. 2F-G), suggesting that Gardner lesions may harbor a relatively more activated CD8 T-cell immune context and potentially more favorable immune surveillance.

We then evaluated the transcriptional shifts of T cells from Gardner and Wishart by measuring their transcriptional similarity using the Bhattacharyya distance. We found large differences in the CD8_naive and CD4_naive cell subgroups (Fig. 2D-G), suggesting that naïve T cells gain distinct cellular functions throughout tumor progression. Further analysis reveals that the downregulated genes in the CD8_naive subgroup from Wishart were enriched in pathways related to T-cell activation, differentiation, and cytokine production (Fig. 2E), whereas those in the CD4_naive subgroup were enriched in apoptosis regulation pathways (Fig. 2G). These findings suggest that, the naïve T cells in Gardner and Wishart exhibit distinctly different patterns and naïve T cells in Gardner showed higher shift capacity from naïve to active effector state.

We also analyzed TCR sequences from scRNA-seq and identified TCRs in 12,792 T cells, including 5302 with clonal expansion and 7490 with unique TCRs (Fig. 2H). Notably, T cells from Gardner exhibited a remarkable capacity for clonal expansion, particularly CD8_GZMK_TXNIP cells, which presented a greater diversity of TCR clones (Fig. 2I and J and Supplementary Fig. 2H). Clone size correlation analysis of the shared TCRs across each pair of CD8$^+$ T-cell clusters confirmed significant and abundant sharing of TCR clonotypes within the CD8_GZMK_CD74 and CD8_GZMK_TXNIP subgroups, indicating dynamic transitions among these clusters in NF2-VS (Fig. 2K). The top TCR clone types in the CD8_GZMK_TXNIP subtype are listed in Supplementary Fig. 2I. Collectively, these results indicate significant differences in CD8 T-cell composition between Gardner and Wishart, with Gardner exhibiting higher proportions of GZMK$^+$ and GZMB$^+$ CD8 T-cell subsets.

The ability of macrophages to promote angiogenesis is greater in Wishart

We identified a total of 59,127 macrophages, which were further categorized into 11 distinct subgroups (Fig. 3A) irrespective of patient origin (Fig. 3B and Supplementary Fig. 3A). The genes highly expressed by different macrophage subgroups are detailed in Fig. 3C and Supplementary Table 3. Interestingly, the distributions of different subpopulations of macrophages revealed distinct patterns in Gardner and Wishart (Supplementary Fig. 3B-C). The Macro_GIMAP4 and Macro_NR4A1 subgroups were more prevalent in Gardner, whereas the Macro_EMP3 subgroup was enriched in Wishart (Fig. 3D-E). Pathway comparative analysis shows that the Macro_EMP3 subpopulation exhibits higher levels of activation in the VEGF pathway, and these cells displays high activity of inflammatory mediators such as IL1A, IL1B, IL6 and TNFα, suggesting that this subgroup may promote an immunosuppressive microenvironment and angiogenesis to facilitate tumor progression (Fig. 3F). Further analysis of HALLMARK pathways (Fig. 3G) revealed that the Macro_EMP3 subgroup displayed increased activity in signaling pathways associated with the Wnt signaling pathway, angiogenesis, and the MTORC1 signaling pathway, further suggesting that this subgroup plays a pivotal role in promoting tumor progression. Conversely, cell populations such as Macro_GIMAP4, Macro_GPNMB, and Macro_TNF, which are more abundant in Gardner, exhibit enhanced antigen presentation, robust immune response activation, and cytokine regulation (Supplementary Fig. 3C). These findings imply that macrophages in Gardner tend to promote antitumor immunity, whereas those in Wishart tend to promote angiogenesis. In addition, we identified the active regulons in these macrophage subpopulations, distinct regulons showed activations in different subpopulations, for example, the IKZF1, a proinflammatory factor, showed higher activation in Macro_TNF (Supplementary Fig. 3D).

The promotion of angiogenesis is a crucial mechanism through which macrophages influence tumor progression. Further comparison of VEGFA expression and immunofluorescence staining (Fig. 3H-I) confirmed elevated levels of VEGF expression in Wishart, providing compelling evidence for the potential efficacy of

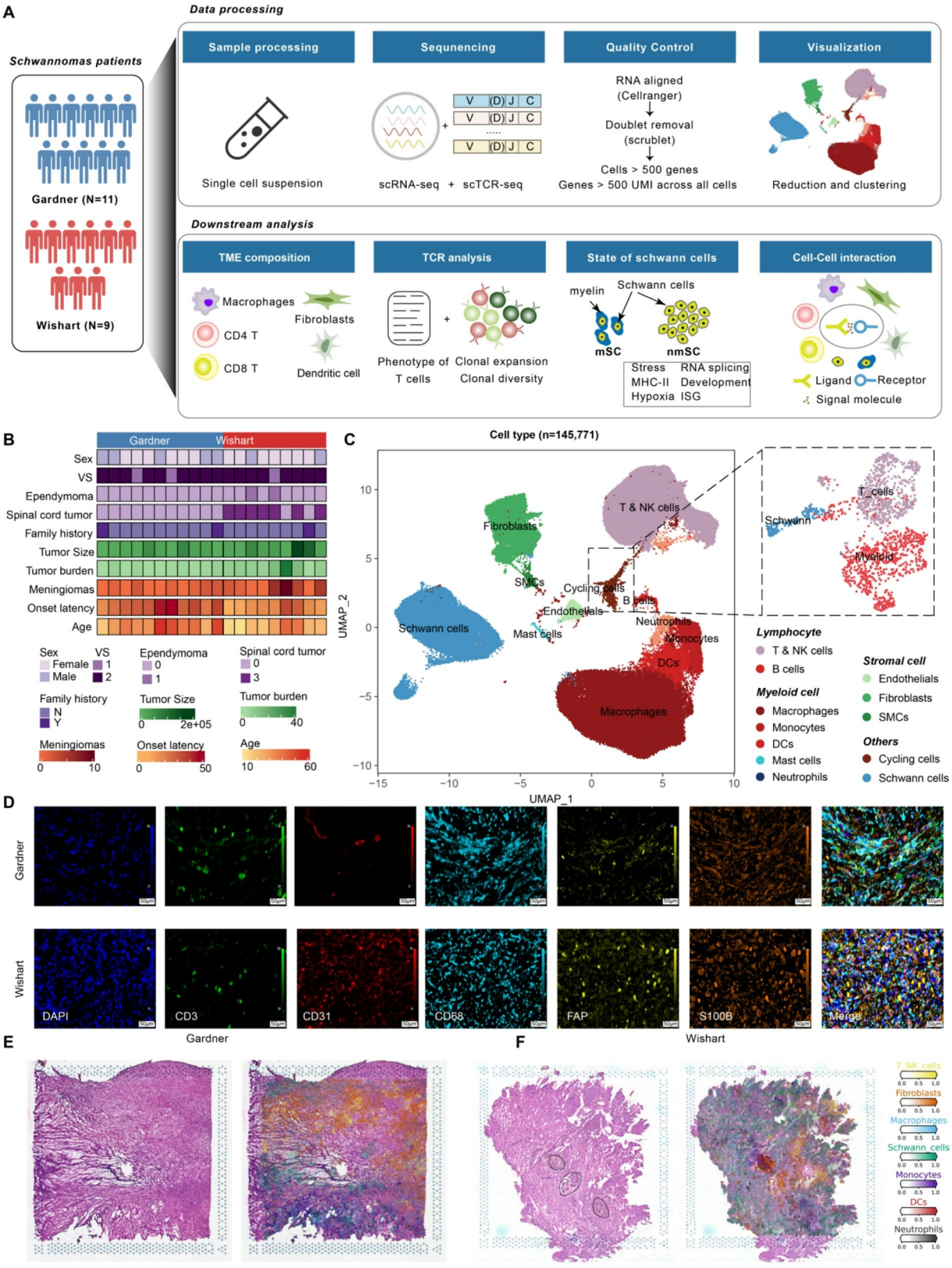

Fig. 1 Overview of cell atlas of NF2-VS patients. **A** Study design and downstream analysis workflow of this cohort. Matched scRNA-seq and scTCR-seq were performed from 11 Gardner and 9 Wishart. **B** Clinical information of patients. **C** UMAP plot showing the cell profiling from the NF2-VS tissue. **D** Multiplex fluorescence showing the cell infiltration of the major celltypes in NF2-VS. CD3, CD31, CD68, FAP, S100B for T cells, endothelial cells, macrophages, fibroblasts and schwann cells, respectively. **E** and **F** Spatial transcriptomics maps of Gardner and Wishart NF2-VS

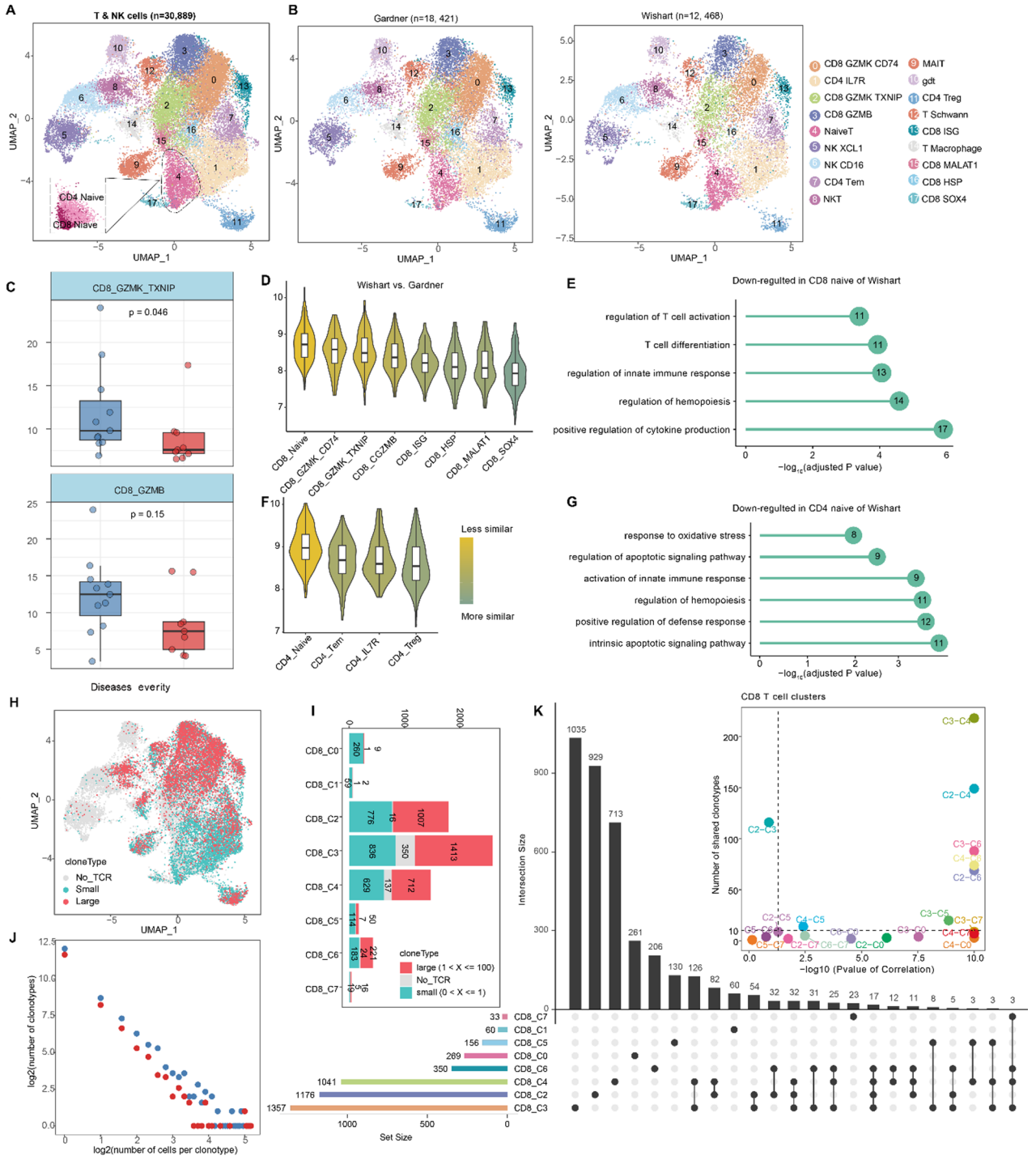

Fig. 2 T cells from Gardner showing higher immune activation and TCR clonality. **A** and **B** UMAP plot of T cells, color-coded by subtypes (**A**) and stratified by disease severity (**B**). **C** Comparison of subtype CD8 GZMK TXNIP and CD8 GZMB between Gardner and Wishart. p-value was calculated by wilcox. test. **D** and **F** Bhattacharyya distance for T subtypes between Gardner and Wishart were calculated, D for CD8 T subtypes and F for CD4 subtypes. **E** and **G** Functional enrichment analysis of down-regulated genes in Wishart CD8 and CD4 subtypes, E for CD8 T cells and G for CD4 T cells. **H** TCR profiling showing the clone size in distinct T subtypes. no_TCR, clone size = 0; small, clone size = 1; large, clone size > = 2. **I** Numbers of clonotype with distinct clone size in different CD8 T subtypes. C0, CD8 naive; C1, CD8 SOX4; C2, CD8 Trm; C3, CD8 GZMK CD74; C4, CD8 GZMK TXNIP; C5, CD8_HSP; C6, CD8 ISG; C7, CD8 MALAT1. **J** The association between the number of T cell clonotypes and the number of cells per clonotype. **K** Upset plot showing the shared TCR clonotype across CD8 subtypes

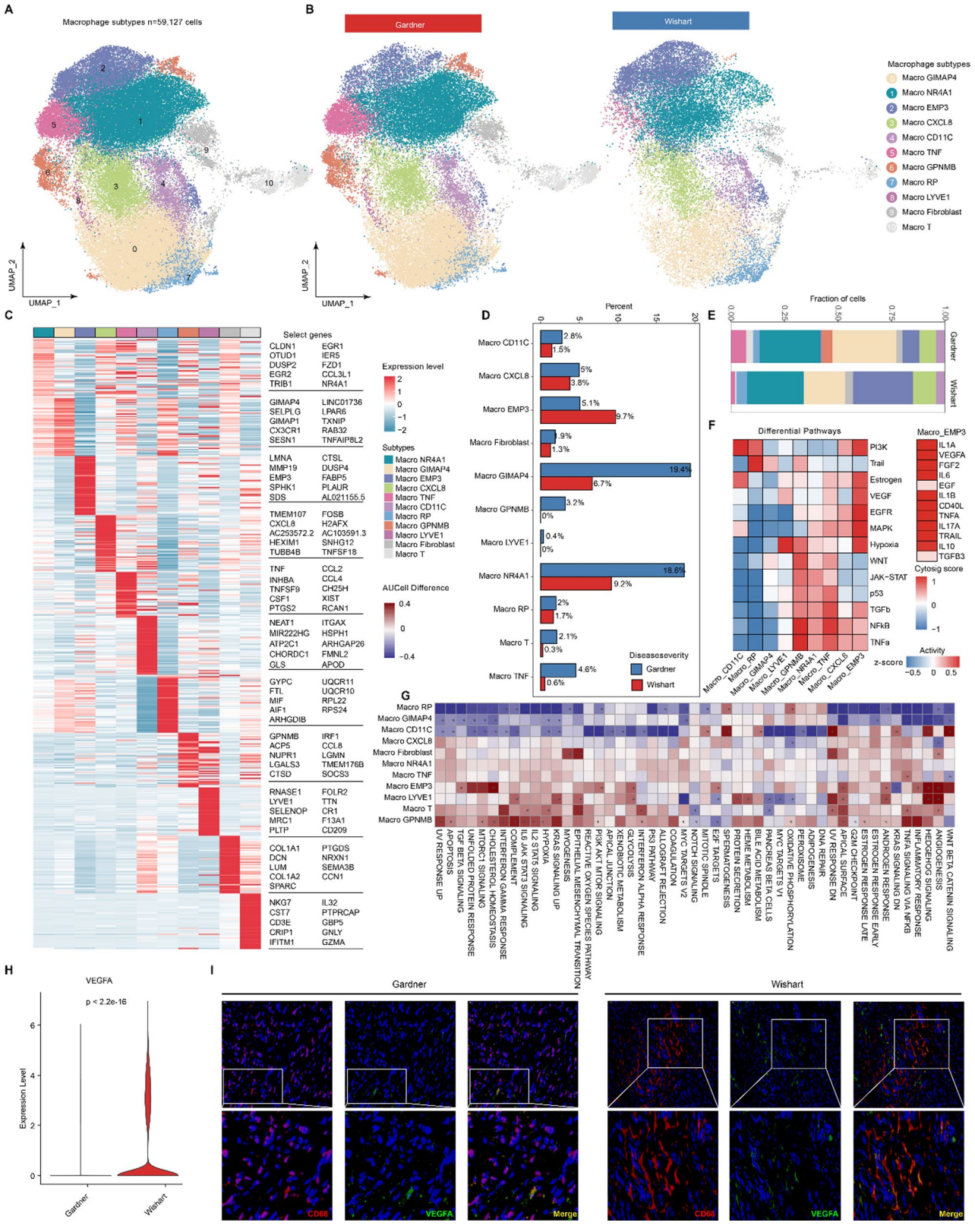

Fig. 3 (See legend on next page.)

(See figure on previous page.)

Fig. 3 A macrophage subtype showing the potential capacity in angiogenesis. **A** and **B** UMAP plot of macrophages, color-coded by subtypes (**A**) and stratified by disease severity (**B**). **C** Expression patterns of subtype specific genes and top 10 genes were labeled. **D** and **E** Proportion of macrophage subtypes between Gardner and Wishart. **F** Pathway enrichment score calculated by progeny (left) and cytokines activation inferred by CytoSig in Macro_EMP3 population (right) (**G**) The log2 fold change of HALLMARK gene set activity was calculated using a one vs. rest comparison strategy, and statistical significance was assessed using the Wilcox.test. P.adjust less than 0.05 were considered statistically significant and were marked with asterisks. **H** Vlnplot showing the expression levels of genes associated with angiogenesis between Gardner and Wishart. **I** Representative images of multiplex fluorescence showing the co-localization of macrophages and VEGFA expression (19003-1-AP, proteintech). Macrophages identified by CD68 staining (sc-20060, Santacruz)

antiangiogenic therapy in NF2-VS [9–12]. Spatial transcriptomic analysis showed that the co-localization of VEGFA and VEGFR was almost absent in Gardner but commonly present in Wishart (Supplementary Fig. 3E). Featureplot also showing the expression of VEGFA and MMP19 across macrophages (Supplementary Fig. 3F). Moreover, we evaluated the developmental potential of each macrophage subpopulation and found that those in Wishart presented significantly greater developmental capabilities (Supplementary Fig. 3G-H). In the TME, macrophages with enhanced developmental potential are more likely to engage in critical processes such as angiogenesis and inflammatory responses, thereby driving tumor development and progression. Therefore, these findings underscore the role of macrophages in Wishart as key facilitators of tumor progression, particularly through the activation of angiogenic pathways.

Fibroblasts are blocked at an early developmental stage and promote collagen deposition in Wishart

We identified four primary fibroblast subgroups (Fig. 4A-B): antigen-presenting CAFs (apCAF), GEM-high expression CAFs (GEM_CAF), ITIH2-high expression CAF (ITIH2_CAF), Matrix CAF (matCAF), based on the expression of canonical gene markers (Supplementary Fig. 4A), along with pericytes showed specific expression of RGS5 (Supplementary Fig. 4B and Supplementary Table 4). Among these four major fibroblast subpopulations, matCAFs were notably enriched in Wishart ($p = 0.04$) (Fig. 4C-D and Supplementary Fig. 4C-E), and these cells exhibit high activity of inflammation-related cytokines, such as FGF2, IL-6, and TGF-β1 (Fig. 4E). Additional GO enrichment analysis of the marker genes of these cells revealed associations with epithelial cell proliferation and wound healing (Fig. 4F and Supplementary Fig. 4F), suggesting that matCAFs may promote tumor cell proliferation by facilitating an immunosuppressive microenvironment and angiogenesis. Furthermore, pathway analysis revealed that, compared with those in Gardner, matCAFs in Wishart presented increased expression of genes involved in tumor-related pathways, such as the MAPK and PI3K-AKT pathways (Fig. 4G), both of which are critical for the development and progression of NF2-VS. The highly active transcription factors in each fibroblast subpopulation were also analyzed. (Fig. 4H). To further substantiate our findings, we also validated the increased proportion of matCAFs in Wishart by examining the expression of α-SMA (Fig. 4I). Further spatial transcriptomics data indicated that COL3A1 also showed higher expression in Wishart (Fig. 4J). Spatial transcriptomic analysis also showed that pericyte marker expression was more prevalent in Wishart (Fig. 4K).

Trajectory analysis of fibroblasts was conducted using Monocle2 combined with scVelo (Fig. 4L). The results revealed a bifurcation in fibroblast differentiation: one branch evolves into apCAFs, which are characterized by their antigen-presenting functions, whereas the other branch transitions toward GEM_CAFs, which are associated with muscle tissue and wound healing functions (Supplementary Fig. 4G). Notably, the matCAF subgroup, which was significantly enriched in Wishart with higher differentiated potential assessed by CytoTRACE (Supplementary Fig. 4H-I), and represented an earlier stage of fibroblast differentiation The expression of CD34, COL15A1, PI16, and DPT, which were identified as the marker of fibroblasts with early differential stage, further confirms the above conclusion (Supplementary Fig. 4J). These findings suggest that the maturation of CAFs in Wishart is impeded at the matCAF stage, leading to excessive stromal deposition. Additionally, CytoTRACE analysis demonstrated that the fibroblast subpopulation in Wishart possesses heightened developmental potential, indicating their important role in the TME and their capacity to promote tumor growth. In summary, these findings underscore the critical role of matCAFs as an essential subpopulation of CAFs that not only increase metastasis but also influence the prognosis of NF2-SWN patients.

Schwann cells exhibit high transcriptional heterogeneity and differential enrichment between Gardner and Wishart

We analyzed the Schwann cell cluster and identified the malignant cell by inferring large-scale copy number variations (CNVs), using immune cells and stromal cells as references (Supplementary Fig. 5A). Upon sub-clustering of the malignant Schwann cells, we identified 8 clusters (Fig. 5A and Supplementary Fig. 5B) on the basis of the expression of canonical gene markers (Fig. 5B, Supplementary Table 5).

By comparing the proportions of different Schwann cell subpopulations, we observed a significant increase

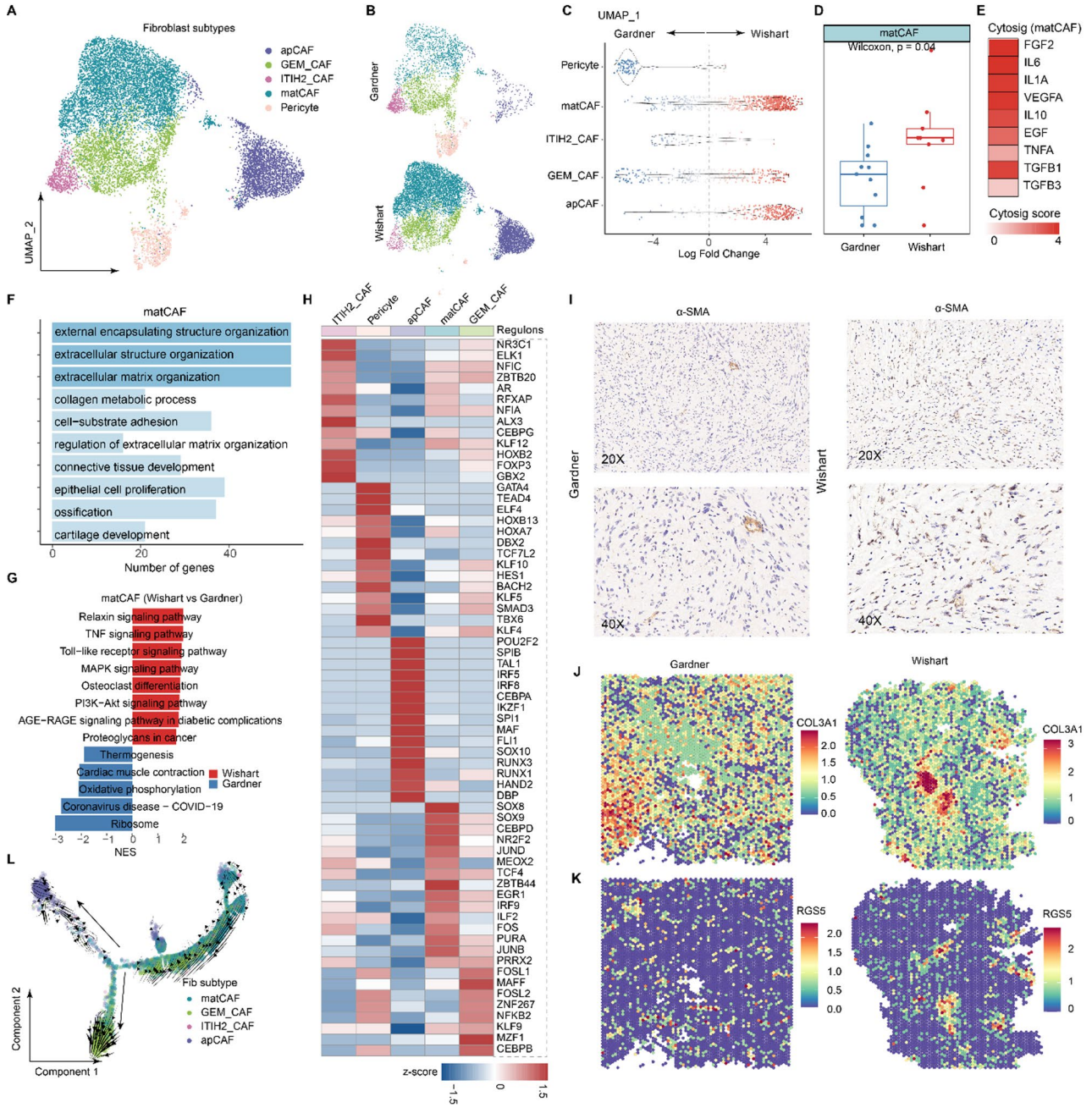

Fig. 4 Fibroblasts showing the enhanced fibrosis in Wishart. **A** and **B** UMAP plot showing the cell profiling of fibroblasts, color-coded by subtypes (**A**) and stratified by disease severity (**B**). **C** Beeswarm plots showing the differential cell abundance compared for Gardner versus Wishart. **D** Comparison of matCAF proportions between Gardner and Wishart. **E** Infered activation of cytokines in matCAF population. **F** and **G** Functional enrichment of genes specific expressed in matCAF, F for GO enrichment and G for KEGG enrichment. **H** TFs were identified using pySCENIC and ranked by RSS score. Top 10 TFS were labeled. **I** Representative images of immunohistochemical showing the degree of α-SMA compared for Gardner versus Wishart. **J** Expression of COL3A1 between Gardner and Wishart in spatial transcriptomics data. **K** Expression of RGS5 between Gardner and Wishart in spatial transcriptomics data. **L** Cell trajectory analysis of fibroblast subtypes using monocle2 and scVelo, colored by subtypes

in the size of the nmSC_FOS subpopulation in Wishart (OR = 1.76, $p < 0.0001$) (Fig. 5C-D), which highly expressed genes associated with stress such as FOS, JUN, JUNB (Fig. 5B), indicated the significance in promoting tumor growth [13]. Whereas the nmSC_ISG15 subpopulation (OR = 1.67, $p < 0.0001$) was predominantly enriched in Gardner (Fig. 5C-D) and showed the higher expression of ISG-related genes such as ISG15, ISG20, MX1(Fig. 5B), suggesting the more active interferon response. Functional enrichment analysis revealed that nmSCs (stress cells) respond primarily to various factors in the TME including the oxidative stress. In contrast, the

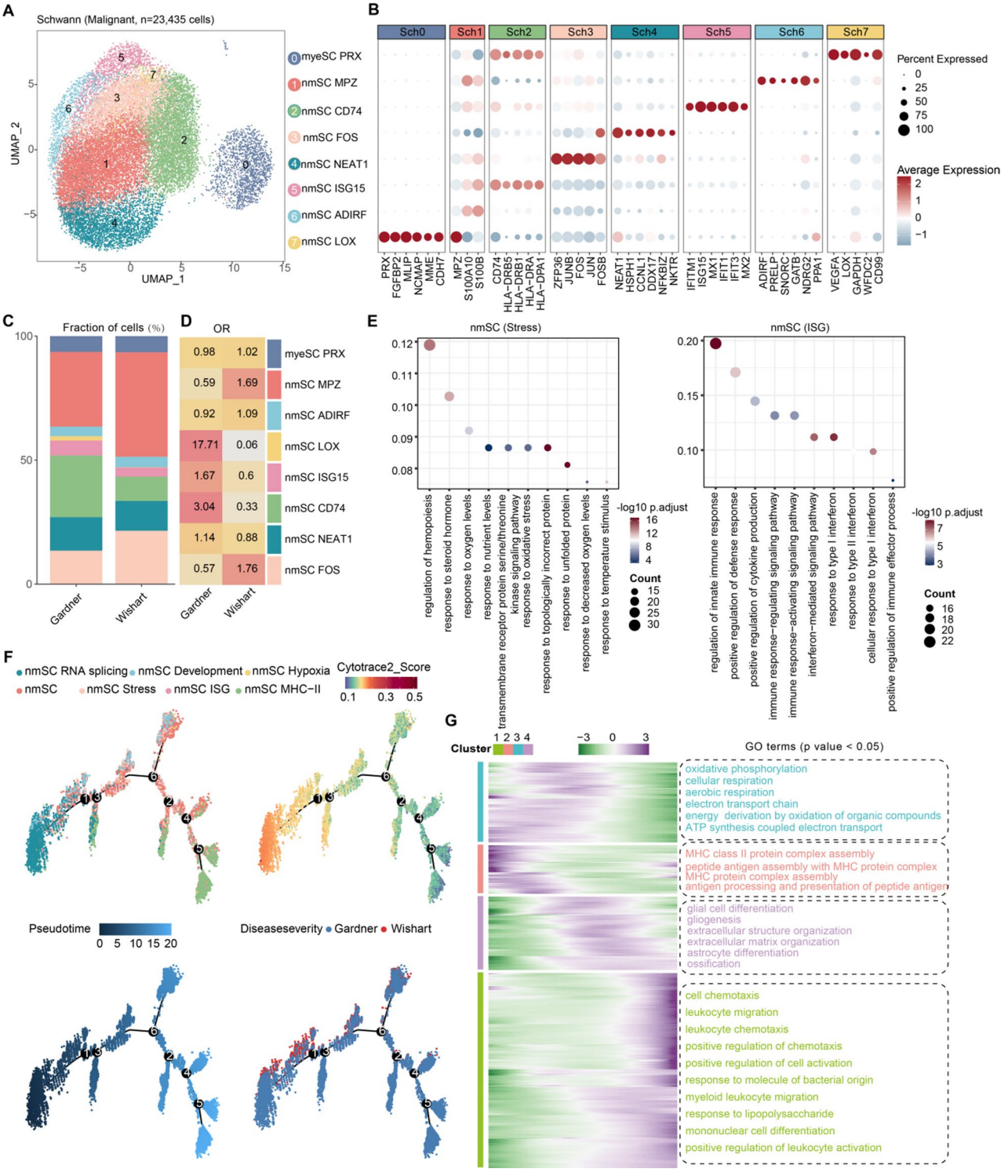

Fig. 5 The Schwann cells exhibit high transcriptional heterogeneity and differential enrichment between Gardner and Wishart. **A** UMAP plot illustrating the distribution of malignant cells, color-coded by subtypes. **B** Expression patterns of canonical markers across subtypes. **C** Comparison of cell fraction in different conditions. **D** Comparison of odds ratio based on cell numbers in different conditions. **E** Functional enrichment analysis of differential expressed genes in special subtypes. **F** Cell trajectory analysis of malignant subtypes, colored by subtypes, CytoTRACE2 score, pseudotime, and conditions. **G** Functional enrichment analysis of differentially expressed genes along pseudotime

nmSC_ISG15 subpopulation is associated primarily with immune responses and cytokine production (Fig. 5E). Pseudotime analysis indicated that the Schwann subpopulation, which expressed genes associated with RNA splicing, served as the starting point of the trajectory. And we found that Schwann cells in Wishart tend to located in the early stages of differentiation, with the primary cellular function being energy derivation, suggesting a blockade of their maturation process (Fig. 5F). Functional enrichment analysis of differentially expressed genes across the Schwann cell differentiation trajectory revealed a sequential shift in cellular function: Schwann cell phenotypes transitioned from states dominated by mitochondrial activity and oxidative phosphorylation to those characterized by extracellular matrix deposition and gliogenesis, ultimately culminating in a phenotype associated with immune cell activation (Fig. 5G). Furthermore, we categorized Schwann cells into two distinct types, myelinating Schwann cells (myeSCs) and non-myelinating Schwann cells (nmSCs), and conducted a comparative analysis between Gardner and Wishart (Supplementary Fig. 5C-H). Both Mye_SC and nmSC showed significant differences between Gardner and Wishart patients. In the Mye_SC sub-population, chemokine expression was higher in Gardner, while matrix-associated genes such as DCN showed elevated expression in Wishart. In the nmSC subgroup, antigen presentation–related genes were highly expressed in Gardner, whereas APOD, DCN, and PTN exhibited increased expression in Wishart. The results revealed intriguing differences in gene expression profiles and function, immune activation was predominant in the Gardner group, whereas higher metabolic activation characterized the Wishart group (Supplementary Fig. 5G-H). These findings underscore the distinct functional characteristics of Schwann cell subtypes in different disease phenotypes, shedding light on their potential contributions to the pathophysiology of NF2-SWN.

The PTN pathway is exclusively activated in Wishart and promotes tumor proliferation

To elucidate the intercellular interactions within NF2-VS, we performed a comprehensive analysis of ligand–receptor signaling on the basis of our scRNA–seq data. Our comparative study revealed that Gardner presented greater quantities and strengths of cellular interactions (Fig. 6A-B and Supplementary Fig. 6A). These dynamic connections predominantly originated from monocytes, smooth muscle cells (SMCs), tumor cells, and macrophages (Fig. 6C). Euclidean distance analysis revealed significant disparities in signaling pathway interactions, particularly those involving IGF and TWEAK, between Gardner and Wishart (Fig. 6D). The signaling networks showed that the IGF exhibited more complex interactions in Gardner via *IGF2 – IGF2R*, *IGF1 – (ITGA6 + ITGB4)* and *IGF2 – (ITGA6 + ITGB4)* (Fig. 6E and G). Whereas, the pathway exhibited a stronger interaction between fibroblasts and tumors in Wishart and *IGF2 – (ITGA6 + ITGB4)* as the dominant ligand-receptor pair (Fig. 6E and G), suggesting a potential role for this interaction in tumor promotion. Pathway TWEAK showed more complex interaction in Gardner and the *TNFSF12 – TNFRSF12A* as the only ligand-receptor pair in Gardner and Wishart (Fig. 6F and H).

Further analysis of the information flow within these signaling pathways revealed that Gardner exhibited a greater number of activated pathways. In contrast, Wishart showed suppressed activity across most pathways. Interestingly, PTN receptor–ligand interactions were exclusively observed in Wishart (Fig. 6I and Supplementary Fig. 6B). Moreover, the PDGF pathway displayed increased interactions between macrophages and fibroblasts in Wishart (Supplementary Fig. 6C), which aligns with the established role of macrophage-derived PDGFB in promoting the survival and proliferation of stromal cells, including fibroblasts [14]. Conversely, the IL16 pathway exhibited more complex interactions among immune cells in Gardner, suggesting a potential antitumor effect (Supplementary Fig. 6D). The results of the analysis of receptor–ligand pairs for several cell subpopulations with enhanced interactions are presented in Supplementary Fig. 6E-G.

Our results indicate that the PTN pathway is exclusively activated in Wishart, with PTN acting as the sole ligand and NCL and SDC2 acting as its receptors (Fig. 6I). Results showed higher PTN expression in Wishart, with colocalization of PTN with SDC2 and NCL (Fig. 6J–L and Supplementary Fig. 6H). Moreover, we found that PTN-positive Schwann cells exhibit a higher cytokine activity, particularly, in Wishart, PTN-positive Schwann cells show high levels of inhibitory cytokine activity, such as IL-10 and TGFB1(Fig. 6M). These inhibitory cytokines can further regulate the induction of a suppressive TME. Additionally, we validated that knocking down *PTN* expression in cells resulted in a marked decrease in schwannoma cell proliferation (Fig. 6N). Collectively, these findings suggest that NF2-VS in Wishart and Gardner exhibit distinct TME. The Gardner phenotype displays enhanced cytotoxic functions, whereas the Wishart phenotype exhibits activated PTN pathway through Schwann cells to modulate the TME, thereby promoting angiogenesis and collagen deposition, which in turn facilitate tumor proliferation (Fig. 6O).

Discussion

In this study, we systematically analyzed and compared the differences in TME between Gardner and Wishart. We found that Gardner exhibit a more favorable TME,

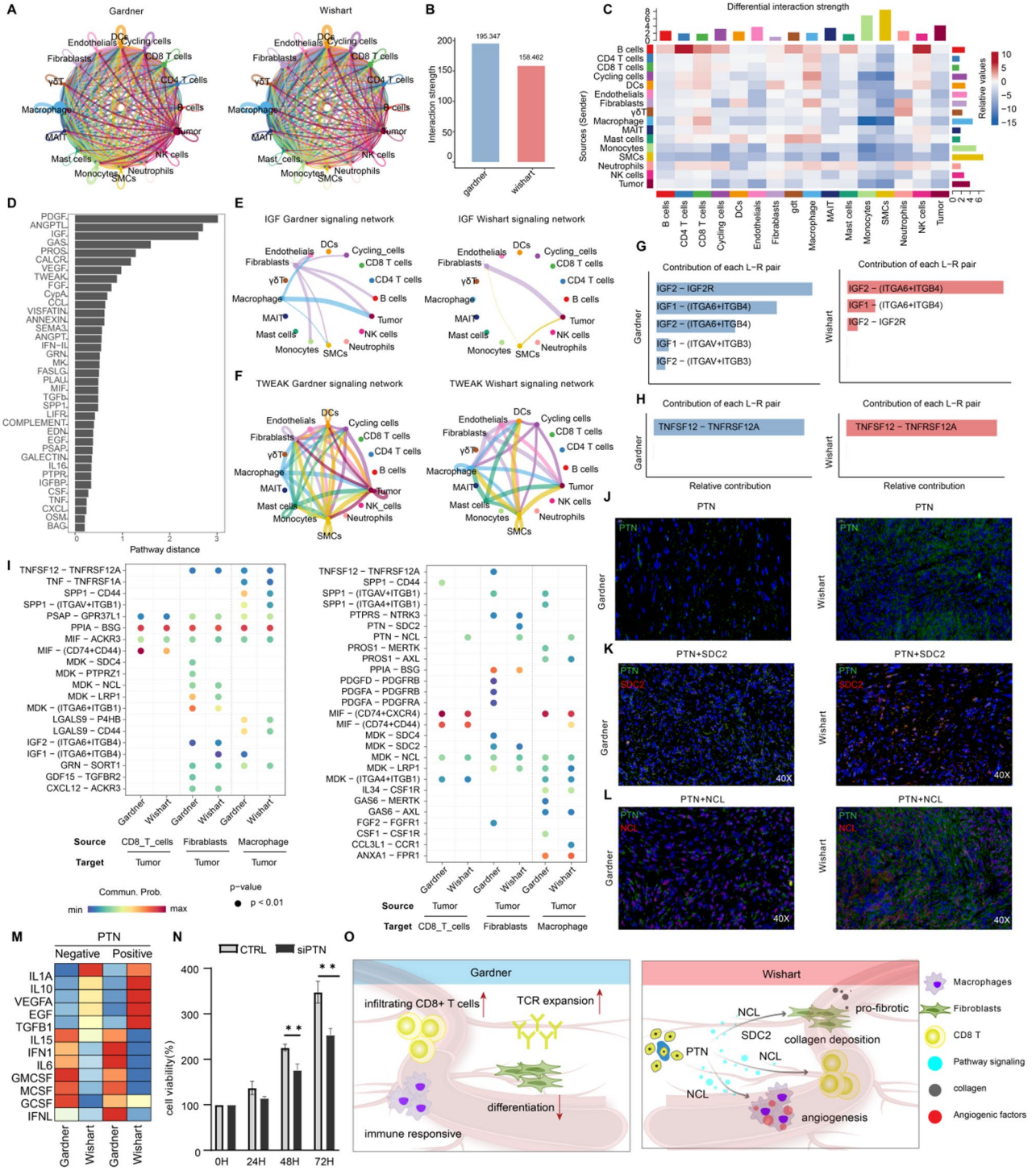

Fig. 6 Cell-cell interaction network analysis. **A** Reconstructed interaction network across celltypes using Cellchat. **B** Comparison of interaction strength between Gardner and Wishart. **C** Differential interaction strength under different conditions. **D** Pathway distance was calculated based on the Euclidean distance between Gardner and Wishart. **E** and **F** Circle plots illustrating the cell-cell interaction network in specific pathways. Edge colors correspond to the sender cell type, and edge weights are proportional to interaction strength, with thicker edges indicating stronger signals. The left panel represents Gardner, while the right panel represents Wishart. **E** IGF pathway; (**F**) TWEAK pathway. **G** and **H** Contribution of each ligand-receptor (L-R) pair in the IGF (**G**) and TWEAK (**H**) pathways. **I** Comparison of communication probabilities mediated by ligand-receptor pairs between CD8 T cells, fibroblasts, and macrophages and tumor groups, in both directions. **J** Immunohistochemical staining of PTN in Gardner (left) and Wishart (right). **K** Fluorescence double staining of PTN and SDC2 protein in Gardner (left) and Wishart (right) patients. **L** Fluorescence double staining of PTN and NCL protein in Gardner (left) and Wishart (right) patients. PTN(green), SDC2(red)) (**M**) Comparison of cytokine activation between Gardner and Wishart groups stratified by PTN expression. **N** Effect of PTN knockdown on tumor cell viability. **O** Summary of key findings

whereas Wishart display a tumor progression-promoting TME. An important finding is that Schwann cells in Wishart can regulate the TME and promote tumor progression by activating the PTN pathway.

Recent findings indicate that *NF2* mutations make Schwann cells hypersensitive to their microenvironment, initiating NF2-VS tumorigenesis [15]. These mutated Schwann cells modulate their surroundings, creating a supportive niche for tumor growth [16]. An analysis of the interactions between malignant Schwann cells and other cells in the TME could lead to new therapeutic strategies for NF2-SWN patients. In our investigation, we examined intercellular interactions through receptor–ligand pair analysis, focusing specifically on how malignant Schwann cells regulate various cell types. Our findings revealed that these malignant Schwann cells regulate three key populations: $CD8^+$ T cells, fibroblasts, and macrophages. Notably, PTN-SDC2 and PTN-NCL interactions were observed exclusively in Wishart. Further analysis and experimental validation demonstrated that Wishart presented increased expression levels of *PTN*, along with pronounced colocalization of PTN with SDC2 and NCL. These findings indicate that in Wishart, Schwann cells utilize PTN to regulate $CD8^+$ T cells, fibroblasts, and macrophages within the TME, thereby promoting an immune landscape that is more conducive to tumor progression.

Studies have shown that PTN is crucial for proliferation, migration, and axonal growth during neural development [17, 18]. Moreover, PTN promoted a striking increase in tumor angiogenesis by binding to SDC2/NCL [19, 20], as well as a remarkable degree of remodeling of the microenvironment [21–23]. Additionally, PTN from Schwann cells may contribute to excessive collagen deposition by fibroblasts in plexiform neurofibromas [24]. Consistent with the above findings, our results show that fibroblasts in Wishart are arrested at the matCAF stage, leading to notable stromal deposition. Macrophages from Wishart exhibit a functional bias toward promoting angiogenesis, accompanied by significantly elevated levels of VEGF expression. PTN-positive Schwann cells from Wishart secrete increased amounts of inhibitory cytokines, thereby modulating the TME. Our cellular experiments also revealed that the proliferation of tumor cells was significantly reduced following *PTN* knockdown. Collectively, these findings underscore the critical role of PTN in the progression of NF2-VS. Further exploration of the regulatory mechanisms of this process could open new therapeutic avenues for the treatment of NF2-VS.

With the deepening research on NF2-SWN, an increasing number of scholars have begun to focus on the TME and the role of immune cells in the occurrence and development of NF2-VS. The study by Amit, M. et al. [25] showed that T cell immunosenescence may be associated with the rapid progression of vestibular schwannoma, providing a theoretical basis for clinical trials evaluating the efficacy of immunotherapy in patients with rapidly progressing vestibular schwannoma. Research by Baruah, P [26]. demonstrated that macrophages are an important component of the vestibular schwannoma stroma. Single-cell RNA sequencing revealed the presence of three distinct macrophage subpopulations within vestibular schwannoma tissues, which may play different roles in the pathogenesis of vestibular schwannoma. More recently, the study by Jones, A.P [27]. used imaging mass cytometry to describe environment-dependent patterns of T cell regulation in NF2-SWN-associated vestibular schwannoma (NF2-SWN VS), proposing that therapies targeting the microenvironment may have potential efficacy against VS. These findings highlight the complexity of VS, the heterogeneity and functional diversity of immune cells in its microenvironment, and also provide support and supplementation for this study's analysis of the disease from the perspective of the immune microenvironment.

However, this study has several limitations. First, the limited sample size restricted our ability to perform subclustering and functional analysis on all cell populations, leading to the exclusion of minor populations with insufficient cell numbers. This constraint hampers our capacity to comprehensively characterize the roles of all subclusters and to delineate the corresponding differences between Gardner and Wishart. In addition, the small sample size has also led to some inconsistencies in the data. For example, our single-cell data showed a higher abundance of pericytes in Gardner, whereas spatial transcriptomic results revealed more prevalent expression of pericyte markers in Wishart. This discrepancy may be driven by the abnormally high expression observed in a single Gardner patient, and expanding the sample size for further analysis is likely to resolve this inconsistency. Second, challenges in obtaining normal tissue samples hindered our ability to conduct comparative analyses of the cellular composition and subgroup proportions between tumor and healthy tissues. Finally, while we identified key factors and interaction networks within the TME through predictive analysis, functional validation experiments and a deeper exploration of their underlying mechanisms remain essential for advancing our understanding. Third, limitations of experimental techniques. The low proportion of tumor SCs in scRNA-seq of NF2 vestibular schwannomas, despite them being the primary tumor component, is mainly due to cell dissociation biases. Tumor SCs are often tightly packed, fragile, or interconnected, making them less likely to survive the enzymatic digestion process compared to robust immune cells, or they may become stuck in cell strainers,

leading to an overrepresentation of stromal and immune cells.

In conclusion, this study systematically analyzes the composition of the TME in different clinical phenotypes of NF2-VS, compares the differences in the TME of Gardner and Wishart, and discusses the possible mechanisms underlying these differences. The results of this study expand our understanding of the TME associated with different clinical types of NF2 tumors and provide a theoretical basis for future immunotherapy based on the TME.

Methods

Clinical samples collection and ethics approval

All procedures involving human participants adhered to the ethical standards of the institution and/or the National Scientific Research Council, in accordance with the 1964 Declaration of Helsinki and its subsequent amendments. This study received approval from the Medical Ethics Committee of Beijing Tiantan Hospital, and written informed consent was obtained from all participants.

All patient specimens were derived from individuals with confirmed NF2-SWN, as diagnosed by neuropathologists at Beijing Tiantan Hospital. The study included 22 NF2-SWN patients who met the Manchester diagnostic criteria for NF2-SWN, presenting with bilateral vestibular schwannomas and meningiomas. Neither patient had undergone prior drug or radiation therapy.

Single-cell RNA-seq data preprocessing and annotation of cell types

To obtain gene expression matrices for cells from patients, we aligned the FASTQ files to the human GRCh38 reference (2020-A version) using the count module of the Cell Ranger pipeline (10X Genomics, default settings, version 6.1.2). For T-cell receptor (TCR) alignment, FASTQ files were mapped to the human vdj-GRCh38 reference (2020-A version) using the vdj module of the Cell Ranger pipeline. The raw spatial expression data was obtained from SpaceRanger output on the 10X Visium platform. Doublets were identified for each sample and removed using Scrublet [28]module in Python 3.9. The expected doublet rate was set to 8% while running the model, and the other parameters were set as 30 principal components (default), and a minimum gene variability of the 85th percentile (default). Cells predicted to be doublets were removed. Further quality control was applied to filter out low-quality cells with either (1) > 6000 or < 500 expressed genes (2) < 500 UMIs (3) > 10% mitochondrial gene counts. Then, R packages harmony [29] was used for integrating the scRNA-seq datasets from multiple samples to remove the batch effects effectively. In brief, the filtered gene expression matrix was then log-normalized and top 3000 highly variable genes were identified for principal component analysis. 30 PC were selected for downstream analysis. Using the the RunHarmony function in R package harmony [29], we integrated the expression matrix from multiple samples. For cell clustering, FindClusters function was used and resolution was set to 0.8, resulted in 29 clusters. 2D UMAP was conducted by RunUMAP function for visualization. Differential gene expression analysis for each cluster was conducted through the Wilcoxon rank sum test, using the FindAllMarkers function. We annotated the resulting clusters into major cell types based on the expression patterns of canonical marker genes, T and NK cells (CD3D, CD3E, NKG7), B cells and plasmas(CD79A, CD79B, MS4A1, MZB1), macrophage cells (C1QA, C1QB, LYZ, CD68, CSF1R), neutrophils (FCGR3B, S100A8, S100A9), monocytes (CD14, FCN1), schwann cells (MPZ, NRXN1, GPM6B), fibroblasts (DCN, COL1A2, COL3A1, COL1A1), and other stromal cells (VWF, PLVAP, ACKR1, CDH5, MYH11, ACTA2).

Malignant identification

To distinguish the malignant cells from schwann cells, the R package Infercnv was used. Prior to running InferCNV [30], macrophages and other myeloid cells were grouped and renamed as "Myeloid cells", T cells and other lymphoid cells as "Lymphoid cells", and fibroblasts along with other stromal cells as "Stromal cells". For each group, 1,000 cells were randomly sampled to construct the reference. All schwann cells were assumed to be potential tumor cells and therefore not included in the reference sets. The inferCNV run() function was executed for each sample with default parameters with the following exceptions: cutoff = 0.1 (recommended for 10X data by inferCNV documentation), HMM = TRUE, HMM_type = 'i3', analysis_mode = 'subclusters', denoise = TRUE. The resulting CNV profiles of both the reference and Schwann cells were subsequently subjected to k-means clustering with the number of clusters (k) set to 7. Schwann cells that clustered together with normal reference cells were classified as malignant.

SCENIC analysis

Gene regulatory networks (GRNs) and transcription factors (TFs) were identified using the pySCENIC [31] workflow with default parameters (https://github.com/aertslab/pySCENIC). The human TF gene list was sourced from the same resource. To rank the genome and link motifs to TF annotations, databases were obtained from cistargetDBs. Differentially activated TFs were identified by applying the Wilcoxon test to the area under the curve (AUC) matrix, allowing the detection of key regulators across different cellular states. TFs specific to particular

cellular states were identified by calculating the RSS score using the R function "calcRSS".

Pathway enrichment analysis

The 50 HALLMARK gene sets for humans were downloaded from the GSEA website (https://www.gsea-msigdb.org/gsea/msigdb). Pathway activity scores for macrophage subtypes were quantified using the R package AUCell [31]. To compare pathway activity differences across subtypes, log2 fold changes were calculated using a one-versus-rest strategy on the basis of AUCell activity matrix. Statistical significance was assessed using the Wilcoxon rank-sum test (Wilcox test), and p-values were adjusted using the false discovery rate (FDR) method. Gene sets with an adjusted p-value < 0.05 and a log2 fold change > 0.25 were considered significantly differentially active. Moreover, R package progeny [32] were used for assessing the activaties of signaling pathways including VEGF, MAPK, Hypoxia, NFκB.

Cytokines inference

To infer cytokine and growth factor signaling activities at the transcriptomic level, we applied CytoSig [33], a signature-based computational framework that estimates cytokine response activities from gene expression profiles. Average normalized gene expression matrices were used as input.

Developmental trajectory inference

Trajectory analysis was performed by monocle2 [34]. The raw count was used to create the object by using the newCellDataSet function and metadata from the Seurat object were added as the phenoData. The DEGs identified by FindAllMarkers in Seurat were set to the ordergene. reduceDimension function was used to reduce dimension with the method "DDRTree". RNA velocity was performed using velocyto and scVelo [35]. We first obtained the loom files that contained raw spliced and unspliced counts from each bam files generated from Cellranger by running the "velocyto run10x" mode based on the human reference genome GRCh38. Next, we merged the loom files of each sample into one loom files and then performed scVelo to calculated the velocity with default parameters and visualize.Moreover, we also used the CytoTRACE 2.0 [36] to predict the developmental potential of cells with the parameter "is_seurat = TRUE".

Immune repertoire analysis

The R package scRepertoire [37] was utilized to identify TCR clonotypes in T cells. To ensure accurate clonotype assignment, only cells containing at least one TCR α-chain (TRA) and one TCR β-chain (TRB) were retained. For T cells with multiple α or β chains, the chain with the highest expression level (based on UMI or read counts) was designated as the dominant α or β chain. A unique clonotype was defined by each dominant α-β chain pair, incorporating both the CDR3 nucleotide sequence and the corresponding rearranged V(D)J genes. T cells sharing the exact same clonotype were considered part of the same T cell clone. Clonotype overlap across different T cell subtypes was visualized using the UpSetR package.

Deconvolution of spatial transcriptome data

To infer the spatial distribution and abundance of different cell types within tissue sections from spatial transcriptomics, we employed the Bayesian-based integration method cell2location. To construct the reference matrix based on scRNAseq data, genes were selected by filter_genes function with the parameters cell_count_cutoff = 5, cell_percentage_cutoff2 = 0.03, and nonz_mean_cutoff = 1.12 and 13,663 genes remained. For reference model training, 250 iterations were performed. Next, cell2location was performed based on the constructed reference matrix, common genes between reference and spatial transcriptome data were retained for model fitting. Abundance matrix of cell types for each spot was generated following 15,000 iterations.

Cell-cell interactions

To construct the intercellular communication network across different cell types, CellChat [38] analysis was performed. Briefly, a log-normalized expression matrix and metadata with cell type labels generated from Seurat were used to create the CellChat object. CellChatDB, a curated database of ligand-receptor interactions in humans and mice, was employed to infer cell-cell communication. Overexpressed ligands and receptors among cell types were identified using the functions identifyOverExpressedGenes and identifyOverExpressedInteractions. The communication probabilities at the signaling pathway level were inferred using the computeCommunProbPathway function.

Multiplex IHC staining

For comprehensive characterization of cell subsets within the TME, we performed multiplex immunofluorescence staining using the PANO 6-plex IHC kit (Panovue, Beijing, China; catalog #0004100100). The staining protocol involved sequential application of different primary antibodies (CD3(ab135372, Abcam), CD31(CST3528, CST), CD68(CST76437, CST), FAP (ab207178, Abcam), S100B (ab52642, Abcam)), followed by incubation with horseradish peroxidase (HRP)-conjugated secondary antibodies and tyramide signal amplification (TSA). Between each TSA cycle, slides underwent microwave treatment to ensure proper antigen retrieval. Following complete labeling of all human antigens, nuclei were

counterstained with 4′,6-diamidino-2-phenylindole (DAPI; Sigma-Aldrich).

Cell experiments

In our cell experiments, we used an immortalized vestibular schwannoma cell line (NF2-VS- Llab-1) derived from NF2-SWN patients, which was developed in our laboratory. PTN gene knockdown was performed using PTN shRNA. Cells were cultured in DMEM medium supplemented with 10% FBS. For the control group, we used NF2-VS-Llab-1 cells transfected with scramble shRNA.

Cell viability assay

Cell viability was measured using the Cell Counting Kit-8 (CCK-8; Dojindo, Kumamoto, Japan). In brief, cells were seeded at a density of 1×10^4 cells per well in 96-well plates. After incubation, 10 µL of CCK-8 solution was added to each well and further incubated at 37 °C for 2 h. Absorbance was then measured at 450 nm using a SpectraMax M5 microplate reader (Molecular Devices, Sunnyvale, CA, USA).

For data normalization, cell viability was calculated as a percentage relative to control cells cultured in lithium-free medium (set as 100%). All experiments were performed in triplicate to ensure reproducibility.

Immunohistochemistry (IHC)

Fresh vestibular schwannoma tissues from NF2-SWN patients were fixed in 4% paraformaldehyde, followed by sequential dehydration in ethanol and paraffin embedding. Tissue Sect. (5 µm thick) were prepared and processed through standard histological procedures, including deparaffinization, rehydration, blocking, and endogenous peroxidase inactivation. For immunohistochemical staining, sections were incubated with primary antibodies overnight at 4 °C. After PBS washing, samples were treated with appropriate secondary antibodies for 1 h at room temperature. Diaminobenzidine (DAB) was used for chromogenic development. Finally, sections were counterstained with hematoxylin and dehydrated through graded ethanol solutions. Stained tissue sections were examined under a light microscope (Olympus Corporation, Tokyo, Japan) at 200× and 400× magnification for histological evaluation.

Statistics

We used R to perform the statistical analysis, Wilcoxon rank-sum test, Pearson, and Fisher's exact test and $P < 0.05$ was considered statistically significant.

Supplementary Information

The online version contains supplementary material available at https://doi.org/10.1186/s12974-026-03799-y.

Supplementary Material 1.

Acknowledgements

This study is supported by the National Natural Science Foundation of China (No.82373451); Beijing Municipal Science and Technology Project (2022) (No. Z221100007422041); the project of scientific research business expenses of provincial research institutes (CZKYF2025-1-B044) ; BTCH 1st Young Talent Enlightenment Program (2024–2026) (to Y.R.); and Natural Science Foundation of Heilongjiang Province (JQ2025C005).

Authors' contributions

P.N.L, J.X., and Y.S.L conceived the project. Y.W., Y.R., Z.J.Y., P.L., and B.W. performed the experiments. G.X., T.P., Y.Z., Y.N.L and Z.Z. analyzed the sequencing data. M.J.Y, C.Z., and X.M. collected clinical samples. Y.W., G.X., P.N.L., J.X., and Y.S.L. wrote the manuscript, with all the authors contributing to writing and providing feedback.

Data availability

The processed single-cell RNA-seq data have been deposited in the Zenodo repository and are accessible at https://doi.org/10.5281/zenodo.15581955. The raw sequencing data generated in our study are available from the corresponding author upon reasonable request. Publicly available packages were used to perform the analysis of scRNA-seq, scTCR and scBCR-seq data. Computer code is available upon reasonable request.

Declarations

Ethics approval and consent to participate

The study was conducted in accordance with the Declaration of Helsinki, and approved by the Ethics Committee of Beijing Tiantan Hospital (KY2019-135-01, 20 May 2020).

Consent for publication

Not applicable.

Competing interests

The authors declare no competing interests.

Author details

[1]Department of Neural Reconstruction, Beijing Neurosurgical Institute, Capital Medical University, Beijing 100070, China
[2]Department of Neurosurgery, Beijing Tiantan Hospital, Capital Medical University, No.119 South Fourth Ring West Road, Fengtai District, Beijing 100070, China
[3]College of Bioinformatics Science and Technology, Harbin Medical University, Harbin, Heilongjiang Province 150081, China
[4]State Key Laboratory of Frigid Zone Cardiovascular Diseases (SKLFZCD), Harbin Medical University, Harbin 150076, China
[5]Department of Neurosurgery, Beijing Tsinghua Changgung Hospital, School of Clinical Medicine, Tsinghua University, Beijing 102218, China
[6]College of Biomedical Information and Engineering, Hainan Medical University, Haikou 571199, China
[7]Interdisciplinary Medicine and Engineering, Harbin Medical University, Harbin, Heilongjiang Province 150081, China
[8]Department of Artificial Intelligence and Biomedical Information, Beijing Neurosurgical Institute, Capital Medical University, Beijing 100070, China
[9]Department of Anesthesiology, The First Affiliated Hospital of Harbin Medical University, Harbin 150081, China
[10]Thoracic Radiotherapy, Harbin Medical University Cancer Hospital, Harbin 150081, China

Received: 21 November 2025 / Accepted: 31 March 2026
Published online: 09 April 2026

References

1. Plotkin SR, Messiaen L, Legius E, Pancza P, Avery RA, Blakeley JO, Babovic-Vuksanovic D, Ferner R, Fisher MJ, Friedman JM, et al. Updated diagnostic criteria

and nomenclature for neurofibromatosis type 2 and schwannomatosis: an international consensus recommendation. Genet Med. 2022;24:1967–77.
2. Coy S, Rashid R, Stemmer-Rachamimov A, Santagata S. An update on the CNS manifestations of neurofibromatosis type 2. Acta Neuropathol. 2020;139:643–65.
3. Baser ME, Friedman JM, Aeschliman D, Joe H, Wallace AJ, Ramsden RT, Evans DG. Predictors of the risk of mortality in neurofibromatosis 2. Am J Hum Genet. 2002;71:715–23.
4. Evans DG, Huson SM, Donnai D, Neary W, Blair V, Newton V, Harris R. A clinical study of type 2 neurofibromatosis. Q J Med. 1992;84:603–18.
5. Dave F, Herrera K, Lockley A, Van De Weijer LL, Henderson S, Sofela AA, Hook L, Adams CL, Ercolano E, Hilton DA, et al. Correction: targeting MERTK on tumour cells and macrophages: a potential intervention for sporadic and NF2-related meningioma and schwannoma tumours. Oncogene. 2024;43:3080.
6. González-Rodriguez MA, Troutman S, Bayle S, Lester DK, Grove M, Duckett D, Kareta MS, Kissil JL. Synergistic effects of combined BET and FAK inhibition against vestibular schwannomas in NF2-related schwannomatosis. Oncogene. 2024;43:2995–3002.
7. Wang Y, Li P, Wang B, Wang S, Liu P. Identification of myeloid-derived suppressor cells that have an immunosuppressive function in NF2 patients. J Cancer Res Clin Oncol. 2019;145:523–33.
8. Wang Y, Zhang C, Yan M, Ma X, Song L, Wang B, Li P, Liu P. PD-L1 regulates tumor proliferation and T-cell function in NF2-associated meningiomas. CNS Neurosci Ther. 2024;30:e14784.
9. Blakeley JO, Ye X, Duda DG, Halpin CF, Bergner AL, Muzikansky A, Merker VL, Gerstner ER, Fayad LM, Ahlawat S, et al. Efficacy and biomarker study of bevacizumab for hearing loss resulting from neurofibromatosis type 2-associated vestibular schwannomas. J Clin Oncol. 2016;34:1669–75.
10. Goutagny S, Raymond E, Sterkers O, Colombani JM, Kalamarides M. Radiographic regression of cranial meningioma in a NF2 patient treated by bevacizumab. Ann Oncol. 2011;22:990–1.
11. Plotkin SR, Allen J, Dhall G, Campian JL, Clapp DW, Fisher MJ, Jain RK, Tonsgard J, Ullrich NJ, Thomas C, et al. Multicenter, prospective, phase II study of maintenance bevacizumab for children and adults with NF2-related schwannomatosis and progressive vestibular schwannoma. Neuro Oncol. 2023;25:1498–506.
12. Tamura R, Yamanobe Y, Fujioka M, Morimoto Y, Fukumura M, Nakaya M, Oishi Y, Sato M, Ueda R, Fujiwara H, et al. Phase I/II study of a vascular endothelial growth factor receptor vaccine in patients with NF2-related schwannomatosis. J Clin Oncol. 2024;42:2578–87.
13. Wu Z, Nicoll M, Ingham RJ. AP-1 family transcription factors: a diverse family of proteins that regulate varied cellular activities in classical hodgkin lymphoma and ALK+ ALCL. Exp Hematol Oncol. 2021;10:4.
14. Zhou X, Franklin RA, Adler M, Jacox JB, Bailis W, Shyer JA, Flavell RA, Mayo A, Alon U, Medzhitov R. Circuit design features of a stable two-cell system. Cell. 2018;172:744–e757717.
15. Vasudevan HN, Lucas CG, Villanueva-Meyer JE, Theodosopoulos PV, Raleigh DR. Genetic events and signaling mechanisms underlying schwann cell fate in development and cancer. Neurosurgery. 2021;88:234–45.
16. Xu D, Yin S, Shu Y. NF2: an underestimated player in cancer metabolic reprogramming and tumor immunity. NPJ Precis Oncol. 2024;8:133.
17. Sun Z, Chen Z, Yin M, Wu X, Guo B, Cheng X, Quan R, Sun Y, Zhang Q, Fan Y, et al. Harnessing developmental dynamics of spinal cord extracellular matrix improves regenerative potential of spinal cord organoids. Cell Stem Cell. 2024;31:772–e787711.
18. Wang X. Pleiotrophin: activity and mechanism. Adv Clin Chem. 2020;98:51–89.
19. Poimenidi E, Theodoropoulou C, Koutsioumpa M, Skondra L, Droggiti E, Van Den Broek M, Koolwijk P, Papadimitriou E. Vascular endothelial growth factor A (VEGF-A) decreases expression and secretion of pleiotrophin in a VEGF receptor-independent manner. Vascul Pharmacol. 2016;80:11–9.
20. Koutsioumpa M, Drosou G, Mikelis C, Theochari K, Vourtsis D, Katsoris P, Giannopoulou E, Courty J, Petrou C, Magafa V, et al. Pleiotrophin expression and role in physiological angiogenesis in vivo: potential involvement of nucleolin. Vasc Cell. 2012;4:4.
21. Perez-Pinera P, Chang Y, Deuel TF. Pleiotrophin, a multifunctional tumor promoter through induction of tumor angiogenesis, remodeling of the tumor microenvironment, and activation of stromal fibroblasts. Cell Cycle. 2007;6:2877–83.
22. Koutsioumpa M, Polytarchou C, Courty J, Zhang Y, Kieffer N, Mikelis C, Skandalis SS, Hellman U, Iliopoulos D, Papadimitriou E. Interplay between alphavbeta3 integrin and nucleolin regulates human endothelial and glioma cell migration. J Biol Chem. 2013;288:343–54.
23. Zhao X, Liu L, Huang Z, Zhu F, Zhang H, Zhou D. PTN from Leydig cells activates SDC2 and modulates human spermatogonial stem cell proliferation and survival via GFRA1. Biol Res. 2024;57:66.
24. Mashour GA, Ratner N, Khan GA, Wang HL, Martuza RL, Kurtz A. The angiogenic factor midkine is aberrantly expressed in NF1-deficient Schwann cells and is a mitogen for neurofibroma-derived cells. Oncogene. 2001;20:97–105.
25. Amit M, Xie T, Gleber-Netto FO, Hunt PJ, Mehta GU, Bell D, Silverman DA, Yaman I, Ye Y, Burks JK, et al. Distinct immune signature predicts progression of vestibular schwannoma and unveils a possible viral etiology. J Exp Clin Cancer Res. 2022;41:292.
26. Baruah P, Mahony C, Marshall JL, Smith CG, Monksfield P, Irving RI, Dumitriu IE, Buckley CD, Croft AP. Single-cell RNA sequencing analysis of vestibular schwannoma reveals functionally distinct macrophage subsets. Br J Cancer. 2024;130:1659–69.
27. Jones AP, Haley MJ, Meadows MH, Gregory GE, Hannan CJ, Simmons AK, Bere LD, Lewis DG, Oliveira P, Smith MJ, et al. Spatial mapping of immune cell environments in NF2-related schwannomatosis vestibular schwannoma. Nat Commun. 2025;16:2944.
28. Wolock SL, Lopez R, Klein AM. Scrublet: computational identification of cell doublets in single-cell transcriptomic data. Cell Syst. 2019;8:281–e291289.
29. Korsunsky I, Millard N, Fan J, Slowikowski K, Zhang F, Wei K, Baglaenko Y, Brenner M, Loh PR, Raychaudhuri S. Fast, sensitive and accurate integration of single-cell data with Harmony. Nat Methods. 2019;16:1289–96.
30. Patel AP, Tirosh I, Trombetta JJ, Shalek AK, Gillespie SM, Wakimoto H, Cahill DP, Nahed BV, Curry WT, Martuza RL, et al. Single-cell RNA-seq highlights intratumoral heterogeneity in primary glioblastoma. Science. 2014;344:1396–401.
31. Aibar S, Gonzalez-Blas CB, Moerman T, Huynh-Thu VA, Imrichova H, Hulselmans G, Rambow F, Marine JC, Geurts P, Aerts J, et al. SCENIC: single-cell regulatory network inference and clustering. Nat Methods. 2017;14:1083–6.
32. Schubert M, Klinger B, Klunemann M, Sieber A, Uhlitz F, Sauer S, Garnett MJ, Bluthgen N, Saez-Rodriguez J. Perturbation-response genes reveal signaling footprints in cancer gene expression. Nat Commun. 2018;9:20.
33. Jiang P, Zhang Y, Ru B, Yang Y, Vu T, Paul R, Mirza A, Altan-Bonnet G, Liu L, Ruppin E, et al. Systematic investigation of cytokine signaling activity at the tissue and single-cell levels. Nat Methods. 2021;18:1181–91.
34. Qiu X, Hill A, Packer J, Lin D, Ma YA, Trapnell C. Single-cell mRNA quantification and differential analysis with Census. Nat Methods. 2017;14:309–15.
35. Bergen V, Lange M, Peidli S, Wolf FA, Theis FJ. Generalizing RNA velocity to transient cell states through dynamical modeling. Nat Biotechnol. 2020;38:1408–14.
36. Kang M, Armenteros JJA, Gulati GS, Gleyzer R, Avagyan S, Brown EL, Zhang W, Usmani A, Earland N, Wu Z et al. Mapping single-cell developmental potential in health and disease with interpretable deep learning. bioRxiv [Preprint]. 2024 Mar 21:2024.03.19.585637. doi: 10.1101/2024.03.19.585637. Update in: Nat Methods. 2025 Nov;22(11):2258-2263. doi: 10.1038/s41592-025-02857-2.
37. Yang Q, Safina KR, Borcherding N. scRepertoire 2: Enhanced and Efficient Toolkit for Single-Cell Immune Profiling. bioRxiv. 2024:2024.2012.2031.630854.
38. Jin S, Guerrero-Juarez CF, Zhang L, Chang I, Ramos R, Kuan CH, Myung P, Plikus MV, Nie Q. Inference and analysis of cell-cell communication using CellChat. Nat Commun. 2021;12:1088.

Publisher's note